

Physicochemical properties and redox behaviour of Fe-doped hybrid nanotubes of the imogolite type and their rGO nanocomposites

*Original*

Physicochemical properties and redox behaviour of Fe-doped hybrid nanotubes of the imogolite type and their rGO nanocomposites / Serrapede, Mara; Rivolo, Paola; Manzoli, Maela; Armandi, Marco; Fontana, Marco; Arcoraci, Davide; Pirri, Candido Fabrizio; Esposito, Serena; Bonelli, Barbara. - In: APPLIED CLAY SCIENCE. - ISSN 0169-1317. - 247:(2024). [10.1016/j.clay.2023.107202]

*Availability:*

This version is available at: 11583/2983645 since: 2023-11-13T10:33:59Z

*Publisher:*

Elsevier

*Published*

DOI:10.1016/j.clay.2023.107202

*Terms of use:*

This article is made available under terms and conditions as specified in the corresponding bibliographic description in the repository

*Publisher copyright*

Elsevier postprint/Author's Accepted Manuscript

© 2024. This manuscript version is made available under the CC-BY-NC-ND 4.0 license  
<http://creativecommons.org/licenses/by-nc-nd/4.0/>. The final authenticated version is available online at:  
<http://dx.doi.org/10.1016/j.clay.2023.107202>

(Article begins on next page)



23           Based on the electrochemical and physicochemical characterizations, nanocomposites of Fe-  
24 doped methylalumogolite and reduced Graphene Oxide (rGO) were obtained for the first time through  
25 a simple method, previously developed by some of us to disperse electrochemically active  
26 nanomaterials onto carbon supports. In the micro/mesoporous nanocomposites (specific surface area  
27 in the 370 - 284 m<sup>2</sup> g<sup>-1</sup> range) the NTs were highly dispersed within the 3D rGO matrix. Cyclic  
28 Voltammetry showed that the capacitive behaviour of the Fe-doped NTs alone were enhanced when  
29 they were embedded in the 3D rGO matrix.

30

31

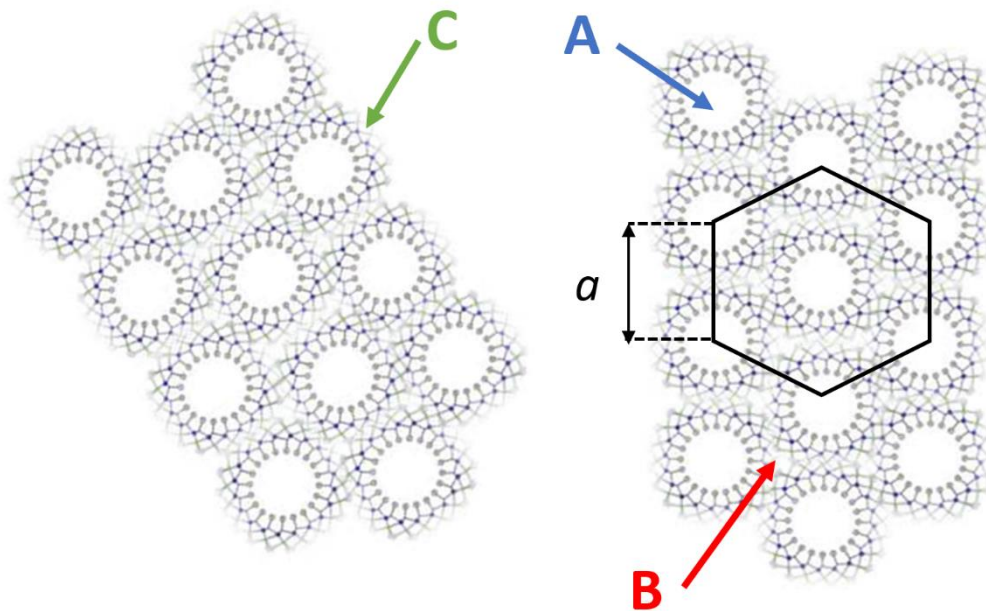
## 1. Introduction

Methylimogolite (MeIMO) is a hybrid material with the chemical formula  $(\text{OH})_3\text{Al}_2\text{O}_3\text{SiCH}_3$ , obtained for the first time by some of the authors of this manuscript (Bottero et al., 2011), occurring as single-walled nanotubes (NTs) characterized by a zig-zag configuration, as reported in an experimental and theoretical study by Monet et al. (Monet et al., 2018).

The hybrid NTs have a hydrophilic outer surface, lined by Al-(OH)-Al and Al-O-Al groups (Fernandez-Martinez and Michot, 2016) and an extremely hydrophobic inner surface, lined by Si- $\text{CH}_3$  groups: the latter is so hydrophobic that water molecules cannot diffuse within preformed MeIMO NTs, as previously shown by SAXS measurements (Nasi et al., 2020).

MeIMO NTs are obtained by a simple, one-pot sol-gel synthesis method (Bottero et al., 2011), and show potentialities in adsorption processes (Bottero et al., 2011; Nasi et al., 2020, Zanzottera et al., 2012a) and heterogeneous catalysis (Shafia et al., 2016; Bahadori et al., 2018). Indeed, the inner surface of MeIMO NTs is accessible to some molecules like methane (Bottero et al., 2011), dichloromethane (Nasi et al., 2020), bromopropanol (Amara et al., 2015) and Nile Red (Picot et al., 2019). The outer surface bears the acid/base properties of proper imogolite NTs, the parent nanomaterial with the chemical formula  $(\text{OH})_3\text{Al}_2\text{O}_3\text{SiOH}$ , as confirmed by the interaction with some probe molecules like carbon dioxide (Zanzottera et al., 2012a), carbon monoxide, ammonia and water vapour (Bonelli et al., 2013a). Imogolite belongs to the allophane family, occurs naturally in volcanic soils, (Yoshinaga and Aomine, 1962) but may be also obtained through sol-gel synthesis (Farmer and Fraser, 1978; Wada et al., 1979; Bonelli et al., 2009). Conversely to MeIMO, proper imogolite is characterized by an extremely hydrophilic inner surface, lined by silanol groups, as shown by both experimental (Bonelli et al., 2009) and theoretical studies (Creton et al., 2008). Drying procedures of proper imogolite NTs may even lead to a deformation of the NTs, as shown in a recent experimental and theoretical study (D'Angelo et al., 2023).

56 Imogolite-like NTs organise into bundles having a pseudo-hexagonal arrangement: Scheme 1  
57 reports, as an example, a sketch of two bundles of imogolite-like NTs to show the three families of  
58 pores occurring in the powder. Such arrangement of NTs allows the formation of B and C pores, in  
59 addition to the proper NTs' pores, namely the A pores, according to the nomenclature proposed by  
60 Ackerman (Ackerman et al., 1993). The A pores are, in turn, characterized by a diameter of ca. 10 Å  
61 and 20 Å in imogolite (Ackerman et al., 1993) and MeIMO (Bottero et al., 2011), respectively. The  
62 pores among three aligned NTs in a bundle (B pores) have a diameter of ca. 3.0 Å and 4.5 Å in  
63 imogolite and MeIMO, respectively. Finally, the slit mesopores among bundles (C pores) have a  
64 broader diameter distribution and have been found to be accessible to larger molecules/ions in both  
65 imogolite (Ackerman et al., 1993) and MeIMO (Nasi et al., 2020), providing a surface that can be  
66 easily functionalized (Zanzottera et al., 2012c) to enhance the possible applications of the NTs in  
67 adsorption/desorption processes, for instance.



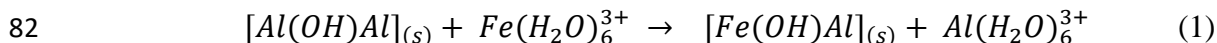
68

69 **Scheme 1.** Sketch of two bundles of imogolite-like NTs and their pseudo-hexagonal arrangement in  
70 powder form (adapted from Ackerman et al. (Ackerman et al., 1993)). The  $a$  parameter is the centre-  
71 to-centre distance between two adjacent NTs.

72

73 As compared to imogolite NTs, the synthesis of MeIMO has a higher yield and leads to  
74 bundles of aligned NTs (Bottero et al., 2011), which are also characterized by higher thermal stability,  
75 larger pore volume and surface area than imogolite NTs (Bonelli et al., 2009).

76 Concerning the C pores, and the related accessible surface, it has been already shown that  
77 octahedral  $Al^{3+}$  ions at the outer surface of both MeIMO and imogolite NTs can be isomorphically  
78 substituted by ions with a proper charge-to-radius ratio, like  $Fe^{3+}$ , by either direct synthesis (i.e. by  
79 adding  $FeCl_3 \cdot 6H_2O$  to the mixture of the aluminium and silicon precursors) or post-synthesis ionic  
80 exchange with  $FeCl_3 \cdot 6H_2O$  in water (Shafia et al., 2015, 2016; Bahadori et al., 2018). The following  
81 reaction occurs (eq. 1):



83

84 In a previous paper concerning the preparation of Fe-doped MeIMO with a maximum Fe  
85 content of 1.4 wt.%, it has been shown that isomorphic substitution of  $Al^{3+}$  at the outer surface of the  
86 NTs can be easily obtained by post-synthesis ionic exchange: the latter is a simpler procedure and  
87 could be used to introduce higher Fe contents as compared to direct synthesis (Bahadori et al., 2018).

88 The Fe-doped MeIMO NTs, already tested in the partial oxidation of tartrazine by  $H_2O_2$  under  
89 UV illumination, were stable to Fe leaching in water (Bahadori et al., 2018) while catalysing a photo-  
90 Fenton reaction. Therefore, our curiosity arose about their possible redox behaviour. Indeed, several  
91 authors have shown that when the total Fe content exceeds 1 wt. % (Shafia et al., 2015), Fe doping  
92 of both MeIMO (Bahadori et al., 2018) and imogolite NTs (Shafia et al., 2016) leads to both  $Al^{3+}/Fe^{3+}$   
93 isomorphic substitution and formation of Fe oxyhydroxide ( $FeOOH$ ) clusters, mostly located at the

94 NTs outer surface (Shafia et al., 2016; Bahadori et al., 2018), due to the natural tendency of Fe to  
95 form Fe-O-Fe bridges (Wang et al., 2002). Moreover, other authors have recently explored the  
96 electrochemical potentialities of Fe-doped imogolite NTs: the latter were able to increase the available  
97 surface area of an electrode and enhance oxygen reduction reaction when Fe phthalocyanines were  
98 adsorbed on the NTs (Castro et al., 2016), showing that imogolite-like nanomaterials have some  
99 electrochemical potentialities, yet partially unexplored.

100 In this work, the FeOOH clusters were obtained on purpose, to have highly dispersed species,  
101 amenable to a redox behaviour, decorating the outer surface of NTs: the FeOOH/NTs interaction is  
102 expected to prevent cluster aggregation, as well as Fe leaching (Bahadori et al., 2018), i.e., two  
103 phenomena that could negatively affect the redox response of the nanomaterial. In previous work, we  
104 have shown that H<sub>2</sub>O molecules cannot enter the extremely hydrophobic inner surface of MeIMO  
105 NTs, even when the powder is resuspended in liquid water (Nasi et al., 2020). To obtain FeOOH-  
106 decorated NTs, we adopted an ionic exchange procedure in water with Fe contents of either 1.4 or  
107 2.8 wt. %. Noticeably, the latter content is twice the amount of Fe that can be obtained by direct  
108 synthesis, while still preserving the NTs (Bahadori et al., 2018). To follow a possible effect of the  
109 ionic exchange procedure on the FeOOH clusters' growth, ionic exchange was performed either by  
110 contacting preformed MeIMO NTs with a 2.8 wt.% Fe aqueous solution or by a two-step exchange  
111 procedure with two (fresh) 1.4 wt.% Fe solutions.

112 The NTs were characterized by complementary physicochemical techniques, namely low  
113 angles X-ray powder diffraction (to study the supramolecular order of NTs forming bundles in the  
114 obtained powder), N<sub>2</sub> sorption at - 196 °C (to determine NTs specific surface area and porosity),  
115 Diffuse Reflectance UV-Vis spectroscopy (to identify both isomorphically substituted Fe<sup>3+</sup> species  
116 and FeOOH clusters), and High-Resolution Transmission Electron Microscopy (HRTEM) analysis,  
117 including EDX elemental mapping, to identify the Fe-containing sites and how they decorate the outer  
118 surface of the NTs. The redox behaviour of Fe-related species was studied by Cyclic Voltammetry.

119 Finally, to improve the NTs' electrochemical response, nanocomposites have been obtained  
120 with reduced Graphene Oxide (rGO) by slightly modifying (the employed synthesis process is  
121 reported in the experimental section, paragraph 2.1.2) a procedure already adopted by some of the  
122 authors of this manuscript to produce nanocomposites of rGO with other types of electrochemically  
123 active compounds (Gigot et al., 2016), suitable for application in energy storage devices (Han et al.,  
124 2014).

125 Since many years, graphene aerogels, variously synthesized (e.g., rGO aerogels), have  
126 attracted a lot of interest (Gorgolis and Galiotis, 2017). Such carbonaceous 3D scaffolds have  
127 fascinating properties, namely the very low density, the high surface area, the thermal resistance and  
128 adsorption capacity, the high mechanical strength and electrical conductivity, and in particular, the  
129 capability to produce the so-called electrochemical double-layer capacitance (EDLC) (Wang et al.,  
130 2021). The intrinsic physico-chemical properties of rGO (and GO) are widely exploited in multiple  
131 applications. Moreover, rGO (and GO) properties are enhanced within composites, for instance with  
132 metal oxides, and are particularly interesting in the field of electrochemistry (supercapacitors) and  
133 catalysis (Tamang et al., 2023). Therefore, after a thorough characterization by Field Emission  
134 Scanning Electron Microscopy (FESEM), HRTEM analysis and N<sub>2</sub> sorption at – 196°, the rGO/NTs  
135 redox behaviour of the nanocomposite of rGO and the NTs at 2.8 wt.% Fe has been assessed by  
136 Cyclic Voltammetry and compared to that of Fe-doped NTs. This is the first report on the synthesis,  
137 physicochemical and electrochemical characterization of Fe-doped methylmorgolite and its  
138 nanocomposites with rGO.

139

## 140 **2. Experimental**

### 141 *2.1 Materials*

142 If not otherwise specified, ACS-grade chemicals were employed (Sigma-Aldrich, Italy).

143 The Graphene Oxide powder (Single Layer GO, 0.7-1.2 nm) was purchased from Cheap  
144 Tubes Inc. – USA).

145

#### 146 *2.1.1 Synthesis and Fe-doping of MeIMO NTs*

147 MeIMO NTs were synthesised according to the method developed by Bottero et al. (Bottero  
148 et al., 2011), by using triethoxymethylsilane (TEMS, 99 %) and aluminium tri-*sec*-butoxide (ATSB,  
149 97%) as Si and Al sources, respectively, in 80 mM HClO<sub>4</sub> solution.

150 Fe-doped MeIMO NTs with either 1.4 wt.% or 2.8 wt.% Fe (chemical formula: (OH)<sub>3</sub>Al<sub>2</sub>-  
151 <sub>x</sub>Fe<sub>x</sub>O<sub>3</sub>SiCH<sub>3</sub> with x = 0.05 and 0.1, respectively) were obtained by post-synthesis ionic exchange,  
152 contacting a preformed MeIMO powder with an aqueous solution of FeCl<sub>3</sub>·6H<sub>2</sub>O (Bahadori et al.,  
153 2018). In a typical synthesis, proper amounts of Me-IMO and FeCl<sub>3</sub>·6H<sub>2</sub>O (97 %) were suspended in  
154 water (resulting pH ≤ 4.0) and maintained under stirring for 24 h. The solid was, then, filtered,  
155 washed, and dried in an oven at 50 °C overnight. Chemical analysis of the transparent supernatant  
156 solution did not detect the presence of residual iron with all the Fe-doped samples. The resulting  
157 sample at 1.4 wt.% Fe will be referred to as Fe1.4-MeIMO.

158 To study the possible effects of the ionic exchange conditions on the growth of the FeOOH  
159 clusters, two samples were obtained at 2.8 wt.% Fe). The former was obtained by contacting the  
160 preformed MeIMO powder with a 2.8 wt.% Fe solution, as described above (sample Fe2.8-MeIMO);  
161 ii) the latter was obtained by contacting the preformed MeIMO powder with a 1.4 wt.% Fe solution,  
162 filtrating and contacting the obtained solid with another 1.4 wt.% Fe fresh solution (Fe1.4x2-  
163 MeIMO).

164

#### 165 *2.1.2 Preparation of the rGO/NTs composites*

166 rGO/NTs composites were produced by mixing two slurries: the former was obtained by  
167 dispersing commercial GO in water ( $2 \text{ mg mL}^{-1}$ ), as reported in ref (Gigot et al., 2016) for the  
168 fabrication of hybrid aerogels; the latter was obtained by dispersing either the Fe1.4-MeIMO or the  
169 Fe2.8-MeIMO NTs in water ( $0.6 \text{ mg mL}^{-1}$ ). Before mixing, each slurry was soaked for 5 h to increase  
170 the powder's wettability. The dispersion obtained by mixing the two slurries (where the Fe-doped  
171 NTs content was 23 wt.%) was sonicated for 5 min, transferred into a Teflon reservoir placed in a  
172 stainless-steel autoclave and heated at  $180 \text{ }^\circ\text{C}$  in an oven for 12 h, to attain hydrothermal reduction  
173 of GO to rGO. The so-produced self-standing rGO hydrogel, embedding the Fe-doped-MeIMO NTs,  
174 was fast-cooled in liquid  $\text{N}_2$  to allow water removal by ultrafast freeze-drying at  $-50 \text{ }^\circ\text{C}$  and residual  
175 pressure of 50 mbar for 12 – 24 h. (Gigot et al., 2016) The obtained nanocomposites will be referred  
176 to as rGO/Fe1.4-MeIMO and rGO/Fe2.8-MeIMO.

177

## 178 *2.2 Methods*

179 Powders X-ray Diffraction (XRD) patterns were measured in the  $2.5 - 18 \text{ } 2\theta$  angles range  
180 ('Xpert Diffractometer using  $\text{Cu K}\alpha$  radiation,  $\lambda = 1.5415 \text{ \AA}$ , step width =  $0.026 \text{ } 2\theta$ , time per step  
181  $2.00 \text{ s}$ ).

182  $\text{N}_2$  adsorption/desorption isotherms were measured at  $-196 \text{ }^\circ\text{C}$  (Quantachrome Autosorb 1C)  
183 on powders previously outgassed either at  $250 \text{ }^\circ\text{C}$  (NTs) or  $150 \text{ }^\circ\text{C}$  (rGO/NTs nanocomposites) to  
184 remove water and other atmospheric contaminants, while preserving the NTs structure and the aerogel  
185 porous structure, respectively (Mackenzie, 1989; Zanzottera et al., 2012b).

186 Diffuse Reflectance (DR) UV-Vis spectra were measured on the NTs pre-outgassed at room  
187 temperature to remove moisture on a Cary 5000 UV-Vis-NIR spectrophotometer (Varian  
188 instruments) equipped with a DR sphere.

189 Electron micrographs were obtained on a high-resolution transmission electron microscope  
190 (HRTEM, Jeol 3010-UHR) operating at 300 kV, equipped with a LaB<sub>6</sub> filament and an Oxford Inca  
191 Energy TEM 300 EDS X-ray analyser (Oxford Link) for atomic recognition. Digital micrographs  
192 were acquired by an Ultrascan 1000 CCD camera and processed by Gatan digital micrograph. Before  
193 measurements, the as-received powder samples were grounded in an agate mortar and deposited on a  
194 copper grid covered with a lacey carbon film. Histograms of the size distribution of the Fe-containing  
195 clusters were obtained by considering a statistically representative number of nanoparticles on the  
196 HRTEM images and the mean particle diameter ( $d_m$ ) of each distribution was calculated according to  
197 eq. 2:

$$198 \quad d_m = \Sigma d_i n_i / \Sigma n_i \quad (2)$$

199 where  $n_i$  is the number of particles of diameter  $d_i$ .

200 The nanocomposite morphology was analysed by using a Field Emission Scanning Electron  
201 Microscope (FESEM Supra 40 manufactured by ZEISS), equipped with an Oxford Si(Li) detector  
202 for Energy Dispersive X-ray analysis (EDX). The samples were observed in their as-prepared form  
203 and no metallization was performed to avoid any surface-morphology modification.

204 The electrochemical characterization of the Fe-doped and undoped MeIMO together with the  
205 rGO/Fe<sub>2.8</sub>MeIMO was performed by using a potentiostat/galvanostat Metrohm Autolab M304 in an  
206 electrochemical cell made of three electrodes in which the reference electrode was an Ag/AgCl  
207 electrode, the counter electrode was platinum and the working electrode consisted of a glassy carbon  
208 electrode of 3 mm diameter covered by the MeIMOs. The measurements were performed in 2.0 M  
209 KOH saturated with nitrogen during the duration of the experiment. Cyclic voltammetry was  
210 performed in the whole potential range of the materials avoiding the evolution of gases.

211

### 212 **3. Results and Discussion**

### 213 3.1 Physico-chemical characterization of MeIMO and Fe-doped MeIMO NTs

214 Figure 1 reports the low-angle XRD patterns (section a) and the N<sub>2</sub> isotherms at -196 °C  
215 (section b) of the undoped and Fe-doped NTs. MeIMO (black curve in Figure 1a) shows the typical  
216 XRD patterns of NTs forming bundles in a pseudo-hexagonal arrangement (Bottero et al., 2011). The  
217 most intense peak at 3.53 2θ is due to the d<sub>100</sub> reflection, from which the parameter *a* corresponding  
218 to the centre-to-centre distance between two aligned NTs within a bundle (Scheme 1) can be  
219 calculated according to eq. 3:

$$220 \quad a = 2d_{100}/\sqrt{3} \quad (3)$$

221 which gives *a* = 28.9 Å for MeIMO. A shoulder to the main peak is observed at ca. 5.68 2θ, assigned  
222 to the d<sub>111</sub> reflection. Such a feature, i.e. a shoulder to the main peak of the d<sub>100</sub> reflection, was already  
223 observed in both natural (Wada et al., 1970) and synthetic imogolite NTs (Farmer and Fraser, 1978).  
224 Several authors who studied proper imogolite NTs (Farmer and Fraser, 1978; Van Der Gaast et al.,  
225 1985) assign such shoulder to the occurrence of a larger number of ordered NTs in a hexagonal close-  
226 packed arrangement (Cradwick et al., 1972). Two (broader) peaks at higher 2θ values at ca. 9.03 and  
227 12.38 2θ angles have been tentatively assigned to the NTs d<sub>001</sub> and d<sub>211</sub> reflections stemming from the  
228 repetition of MeIMO structural units along the NTs, according to similar XRD diffraction of powder  
229 samples of MeIMO obtained by the same procedure (Bottero et al., 2011). The peaks assignment is,  
230 however, controversial, based on the recent literature reporting, *inter alia*, scattering experiments  
231 with imogolite-like nanomaterials of various origins and compositions (Monet et al., 2018; D'Angelo  
232 et al., 2023). Concerning the main peaks, modulations should be indexed with only two *hk* indices,  
233 therefore, the first peak should be indexed as a 10 peak, the second peak as an 11 peak and the d<sub>001</sub>  
234 peak should be extinguished (Monet et al., 2018; D'Angelo et al., 2023).

235 The XRD pattern of the Fe<sub>1.4</sub>-MeIMO sample does not show substantial differences from  
236 that of the parent MeIMO, in agreement with the limited Fe content (Bahadori et al., 2018).

237 Conversely, the two samples at 2.8 wt.% Fe have different XRD patterns, in that the  $d_{100}$  reflection  
238 shifts to higher  $2\theta$  values, becoming broader and more intense, finally hampering the calculation of  
239 the  $a$  parameter. This phenomenon can be ascribed to a change in the ordering of NTs upon ionic  
240 exchange with 2.8 wt.% Fe, which induces non-negligible changes in the alignment of the NTs in the  
241 final material in powder form, since the presence of Fe-oxyhydroxides species of different sizes (*vide*  
242 *infra*) at the outer surface of the NTs should perturb their successive organization into bundles when  
243 powders are obtained. The same phenomenon could also be responsible for the appearance of new  
244 pores, with a diameter of ca. 10 Å (*vide infra*), in the samples at 2.8 wt.% Fe. It must be remarked  
245 that the adopted XRD sample holder did not allow a more accurate determination of the  $d_{100}$  peak  
246 position (due to the small amount of the available powders at 2.8 wt.% Fe), however, the HRTEM  
247 inspection allowed us to infer more details about the formation of NTs bundles (*vide infra*).

248

249

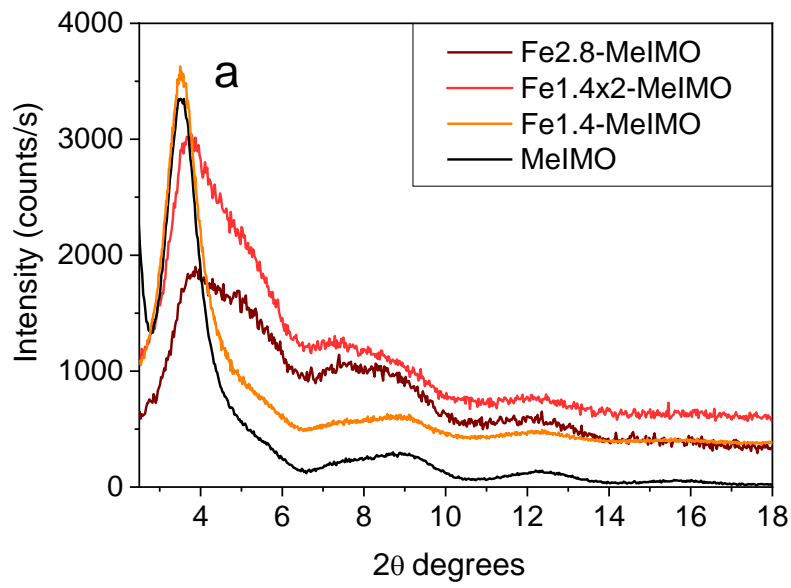
250

251

252

253

254



255

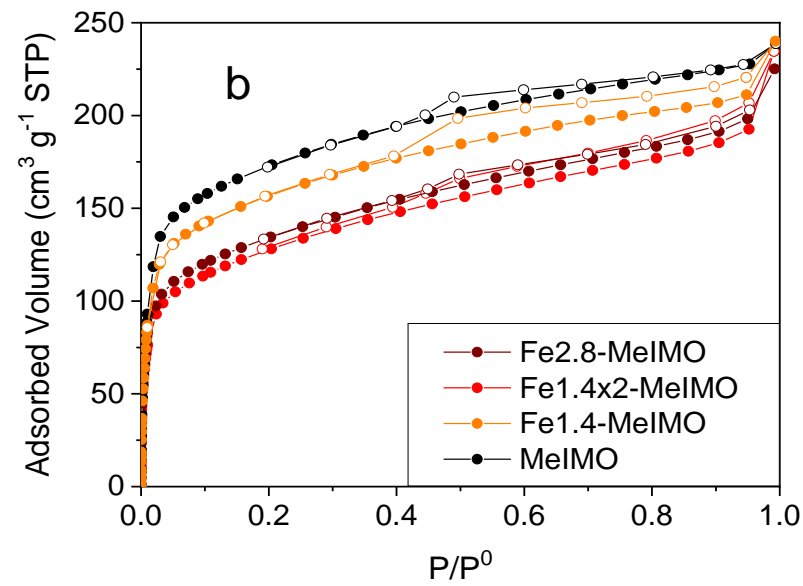
256

257

258

259

260



261

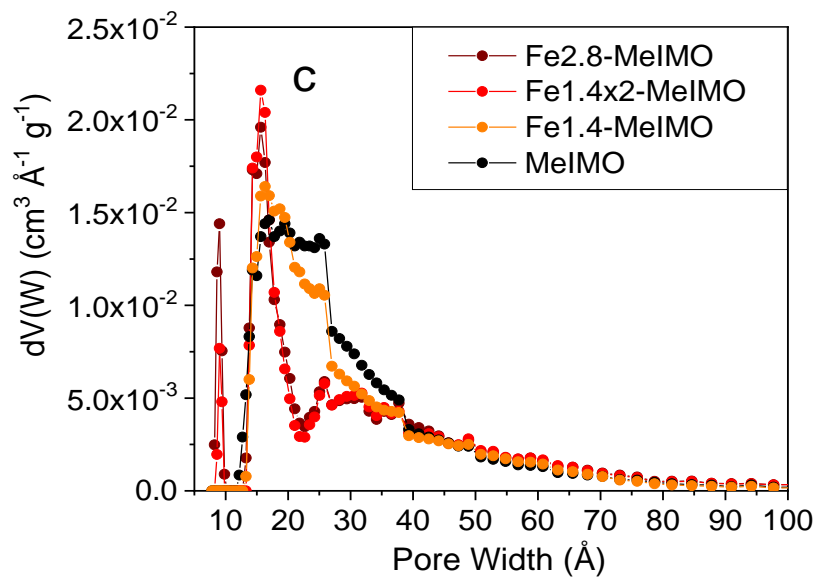
262

263

264

265

266



267

268 **Figure 1.** Low angles XRD patterns (a), N<sub>2</sub> isotherms at -196 °C (b) and PSD curves (c) of the  
269 following samples: MeIMO (black curves), Fe1.4-MeIMO (orange curves), Fe1.4x2-MeIMO (red  
270 curves) and Fe2.8-MeIMO (brown curves).

271

272 Figure 1b reports the N<sub>2</sub> isotherms at -196 °C of both undoped and Fe-doped MeIMO NTs: the four  
273 samples show Type IV isotherms, proper of microporous materials with some mesoporosity  
274 (Armandi et al., 2008; Thommes et al., 2015). The H4 hysteresis loop observed in all the isotherms  
275 is typical of slit/wedge-shaped pores, likely forming among the bundles (Scheme 1). The values of  
276 Brunauer-Emmett-Teller Specific Surface Area (BET SSA) in Table 1 show that Fe-doping leads to  
277 a progressive, but limited, decrease of the SSA. The curves of the corresponding Pore Size  
278 Distribution (PSD) (Figure 1c) show that the nanomaterials' porosity is strongly affected by ionic  
279 exchange in different ways. Concerning mesopores, Fe-exchange brings about a decrease in the  
280 number of pores in the 20 – 40 Å range: indeed, the formation of Fe-oxyhydroxide clusters at the NTs  
281 outer surface could affect the (larger) mesopores occurring between bundles, namely the C pores in  
282 Scheme 1. Concerning micropores, at 2.8 wt.% Fe a new family of micropores shows up with a  
283 diameter of ca. 10 Å, which could be due to a “new” porosity, absent at lower Fe content, due to the  
284 occurrence of Fe-oxyhydroxide clusters at the outer surface of the NTs that affect the subsequent  
285 formation of bundles in the powder and the packing of the Fe-doped NTs at higher Fe content.

286 Fe doping leads to a slight decrease in the samples' microporous volume, with the likely  
287 exception of the Fe2.8-MeIMO sample. The difference in the microporous volume between the two  
288 samples at 2.8 wt.% Fe (Fe1.4x-MeIMO and Fe2.8-MeIMO) may indicate that the two synthesis  
289 procedures slightly affect the samples' textural properties, although they could also lead to different  
290 clusters' growth, which was further investigated by HRTEM (*vide infra*).

291

292 **Table 1.** Nominal Fe content, relevant textural properties, and bandgap energy ( $E_g$ , eV) of the  
 293 studied samples.

Sample (Nominal wt.% Fe)	Chemical formula	BET SSA ( $\text{m}^2 \text{g}^{-1}$ )	Total pore volume ( $\text{cm}^3 \text{g}^{-1}$ )	Bandgap energy (eV) <sup>b</sup>
		Micropore area <sup>a</sup> ( $\text{m}^2 \text{g}^{-1}$ )	Micropore volume <sup>a</sup> ( $\text{cm}^3 \text{g}^{-1}$ )	
MeIMO (0)	$(\text{OH})_3\text{Al}_2\text{O}_3\text{SiCH}_3$	615	0.35	4.9
		336	0.14	
Fe1.4-MeIMO (1.4)	$(\text{OH})_3\text{Al}_{1.95}\text{Fe}_{0.05}\text{O}_3\text{SiCH}_3$	560	0.33	2.4
		240	0.10	
Fe1.4x2-MeIMO (2.8)	$(\text{OH})_3\text{Al}_{1.9}\text{Fe}_{0.1}\text{O}_3\text{SiCH}_3$	455	0.29	2.3
		217	0.09	
Fe2.8-MeIMO (2.8)	$(\text{OH})_3\text{Al}_{1.9}\text{Fe}_{0.1}\text{O}_3\text{SiCH}_3$	478	0.31	2.3
		245	0.16	

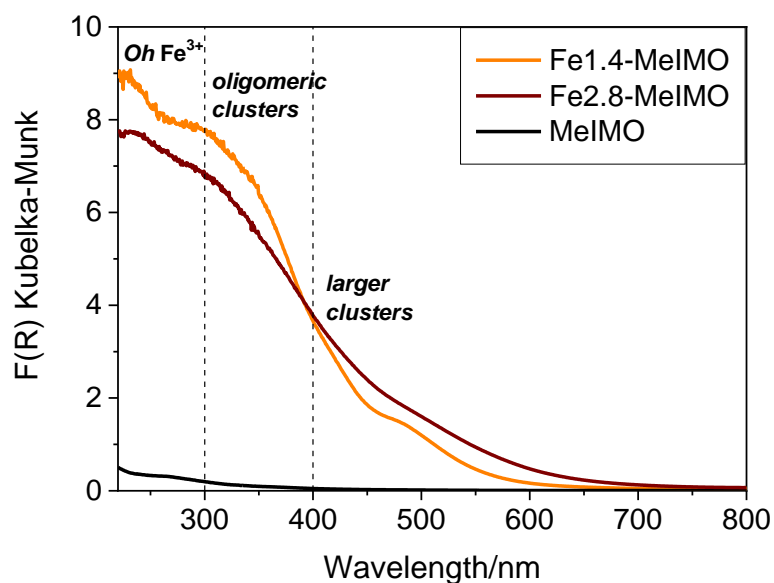
294 <sup>a</sup> As determined by applying the *t*-plot method.

295 <sup>b</sup> As determined by applying the Tauc plot method for an indirect semiconductor to the DR-UV-Vis  
 296 spectra.

297

298 Further insight into the effect of Fe-doping can be derived by the DR UV-Vis spectra reported  
 299 in Figure 2: MeIMO (black curve) has, as expected, a negligible absorption in the UV-vis range,  
 300 whereas the Fe-doped samples show intense and broad absorption bands both below and above 300  
 301 nm. Below 300 nm, two bands at ca. 235 and 290 nm are ascribed to charge transfer (CT) transitions  
 302 from  $\text{O}^{2-}$  to isolated  $\text{Fe}^{3+}$  ions, as observed in other Fe-doped alumino-silicate systems, namely Fe-  
 303 exchanged zeolites (Kumar et al., 2006; Iwasaki et al., 2008; Ma et al., 2012).

304



305

306 **Figure 2.** DR UV-Vis spectra of the following samples: MeIMO (black curve), Fe1.4-MeIMO  
 307 (orange curve) and Fe2.8-MeIMO (brown curve).

308

309 At variance with zeolites, the formation of tetrahedral  $\text{Fe}^{3+}$  sites (band at 235 nm) is unlikely  
 310 here, and both bands are assigned to  $\text{Fe}^{3+}$  ions in likely octahedral (*Oh*) coordination. Indeed, the  
 311 conditions adopted during the ionic exchange in water lead us to exclude the assignment of the band  
 312 at 235 nm to CT to tetrahedral  $\text{Fe}^{3+}$  species, although previous calculations on similar systems showed  
 313 that they could occur as defects at the inner and outer surface of the NTs (Teobaldi et al., 2008).  
 314 Therefore, the 235 nm band can be due to some  $\text{Fe}^{3+}$  in defective sites, i.e. in a different environment  
 315 as compared to the *Oh* species deriving from reaction (1), absorbing at 290 nm. The absorption above  
 316 300 nm is complex. According to the literature, Fe oxyhydroxide clusters of different dimensions  
 317 absorb at different wavelengths (Kumar et al., 2006; Iwasaki et al., 2008; Ma et al., 2012; Bahadori  
 318 et al., 2018). More specifically, larger clusters absorb above 400 nm, therefore bands in the 300–400  
 319 nm range are assigned to CT transitions in smaller (oligomeric) Fe oxyhydroxide clusters, whereas  
 320 bands above 400 nm are ascribed to larger (nm range) Fe oxyhydroxide particles and *d-d* transitions

321 (Kumar et al., 2006; Iwasaki et al., 2008; Ma et al., 2012; Bahadori et al., 2018). Interestingly, the  
322 bands have different relative intensities with the samples (the spectrum of the Fe<sub>1.4x2</sub>-MeIMO  
323 sample was practically superimposable to that of Fe<sub>2.8</sub>-MeIMO and was not reported for clarity).  
324 Accordingly, at higher Fe content, the bands due to oligomeric species become less intense, whereas  
325 the absorption due to larger clusters increases in intensity and becomes broader.

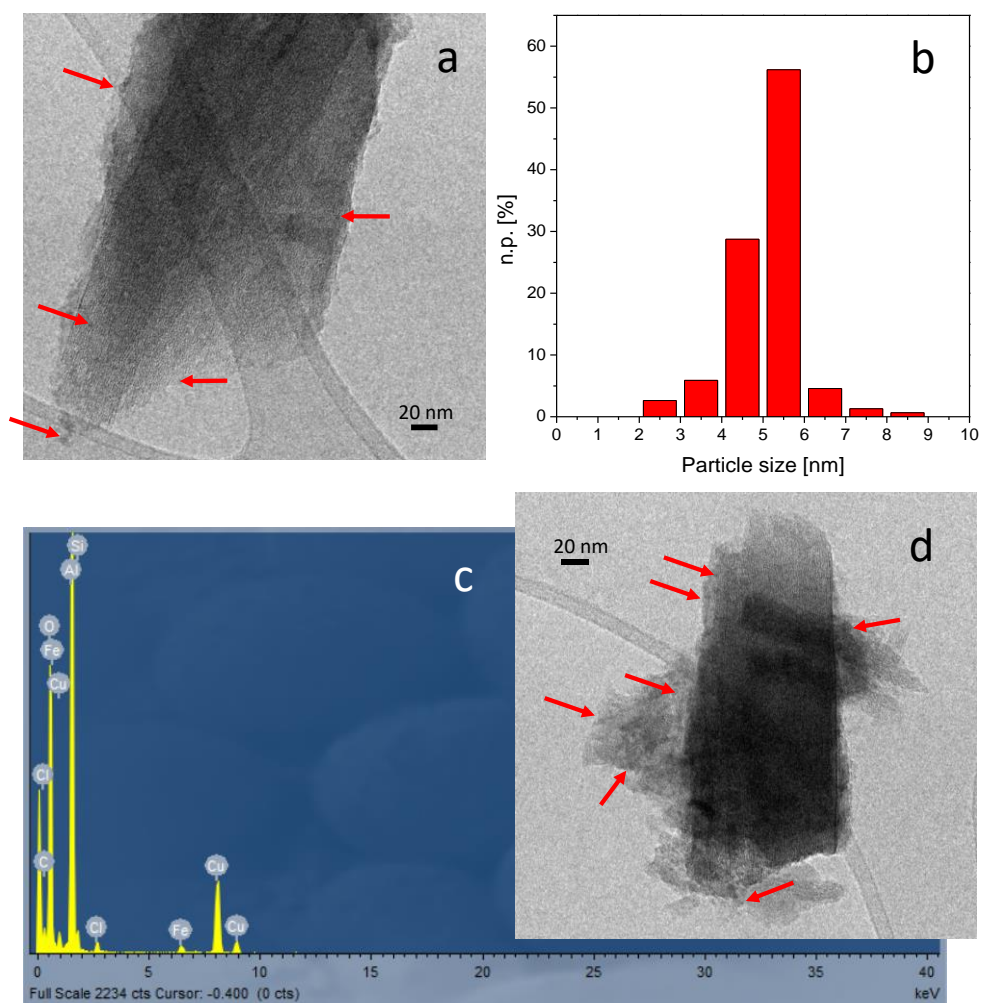
326 By applying Tauc's plot method, the NTs bandgap energy values in Table 1 have been  
327 determined. As expected, MeIMO is an insulator, with a bandgap of 4.9 eV, in agreement with  
328 theoretical results (Alvarez-Ramírez, 2009), but doping with Fe turns the NTs into a semiconductor  
329 with a bandgap of 2.3 - 2.4 eV. Interestingly, increasing the Fe content to 2.8 wt.% does not contribute  
330 to a remarkable decrease in the bandgap, as compared to 1.4 wt. % Fe. As demonstrated by several  
331 authors (Avellan et al., 2014; Shafia et al., 2015; Bahadori et al., 2018), the isomorphic substitution  
332 of Al<sup>3+</sup> by Fe<sup>3+</sup> in imogolite-like NTs hardly exceeds 1.0 wt.% Fe. However, increasing the Fe content  
333 could affect the growth of the Fe-oxyhydroxide clusters. Consequently, the bandgap energy decreases  
334 to a certain extent, due to the Al<sup>3+</sup>/Fe<sup>3+</sup> isomorphic substitution, but higher Fe contents mainly lead  
335 either to the growth of preformed Fe-oxyhydroxide clusters or to the growth of new clusters around  
336 isomorphically substituted Fe<sup>3+</sup> sites, acting as "crystalline seeds".

337 To unravel the effect of Fe-doping on the growth of Fe-containing species as a consequence  
338 of the different ionic exchange procedures, a careful HRTEM characterization combined with EDX  
339 analysis was carried out on both the Fe<sub>1.4x2</sub>-MeIMO and Fe<sub>2.8</sub>-MeIMO samples.

340 Concerning morphology, in a previous paper (Bottero et al., 2011) it was shown that MeIMO  
341 forms bundles of closely packed NTs. First, independently from the Fe amount and the adopted  
342 doping procedure, the morphological features of bare MeIMO NTs were maintained upon Fe insertion  
343 (Figures 3 and 4). Moreover, Fe species, likely Fe-oxyhydroxide clusters, were observed at the outer  
344 surface of the NTs (indicated by arrows in Figures 3a, 3d, and Figures 4a, 4b) and no cluster  
345 agglomerates were observed. The clusters' size was evaluated by considering electron micrographs

346 acquired at least at 50,000× magnification, where the Fe-oxyhydroxide clusters, well contrasted as  
347 compared to the MeIMO structure, were detected. Highly dispersed Fe-containing species were  
348 observed in both samples, having a mean diameter  $d_m = 4.9 \pm 0.9$  nm in Fe1.4x2-MeIMO and  $d_m = 5.1$   
349  $\pm 0.8$  nm in Fe2.8-MeIMO. This fact agrees with the DR UV-Vis spectra (Figure 2), showing the  
350 occurrence of both oligomeric and larger FeOOH clusters. Despite the similar mean diameters of the  
351 clusters, their size distribution was broader with the Fe1.4x2-MeIMO sample (ranging between 2 and  
352 9 nm) as compared to the Fe2.8-MeIMO sample (ranging from 3 to 8 nm). These features indicate  
353 that the adopted doping procedures did not affect much the average size of the clusters, but the double  
354 exchange procedure led to a broader size distribution of the latter species. Moreover, it may indicate  
355 that if the double exchange is carried out, besides increasing the size of pre-formed clusters, new  
356 clusters form, confirming that it is very difficult to control the extent of isomorphic substitution versus  
357 cluster growth, as both processes unavoidably occur by ionic exchange.

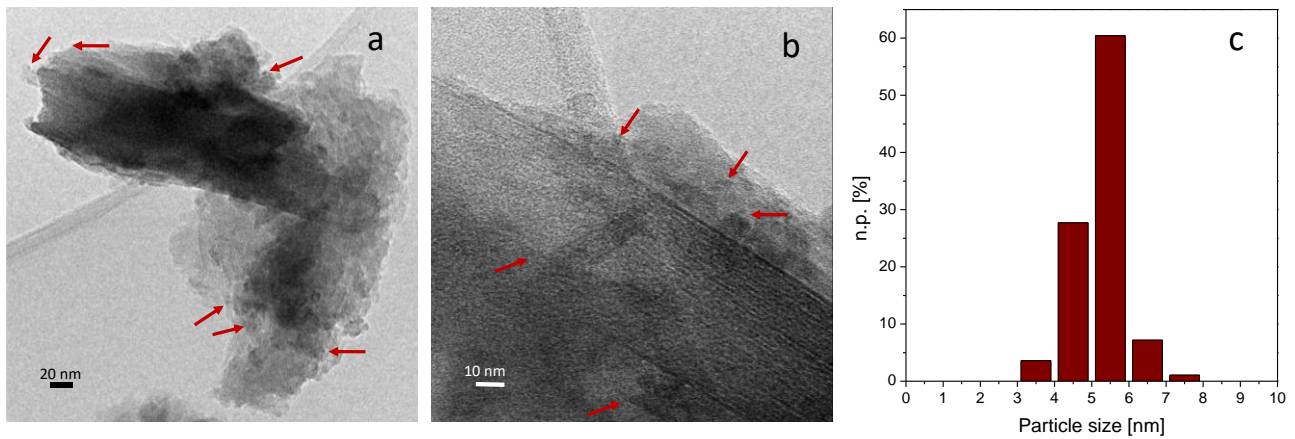
358



359

360 **Figure 3.** HRTEM representative images of Fe<sub>1.4x2</sub>-MeIMO in which the bundles formed by parallel  
 361 NTs can be observed (a, d). Particle size distribution of Fe oxo-hydroxide clusters (b) and EDX  
 362 spectrum of the region shown in d (c). Instrumental magnification 50,000×. The Fe-containing species  
 363 are highlighted by red arrows. In the EDX spectrum, the lines of Cl and Cu are due to the adopted Fe  
 364 precursor and the sample holder, respectively.

365



366

367 **Figure 4.** HRTEM representative images of Fe<sub>2.8</sub>-MeIMO bundles (a) formed by parallel NTs (b).

368 Particle size distribution of Fe oxo-hydroxide clusters (c). Instrumental magnification is 50,000× and

369 150,000×, respectively. The Fe-containing species are highlighted by brown arrows.

370

### 371 3.2 Physico-chemical characterization of the rGO/NTs nanocomposites

372 On the ground of the previously described physicochemical characterization, rGO/NTs

373 nanocomposites were produced with the Fe<sub>1.4</sub>-MeIMO and the Fe<sub>2.8</sub>-MeIMO samples. Figure 5

374 reports some selected micrographs obtained by FESEM inspection of the parent rGO and the

375 rGO/Fe<sub>1.4</sub>-MeIMO nanocomposite: in Figure 5a, wrinkled and curled-up rGO flakes, typical of the

376 adopted preparation procedure (Gigot et al., 2016), are observed, giving rise to a 3D highly porous

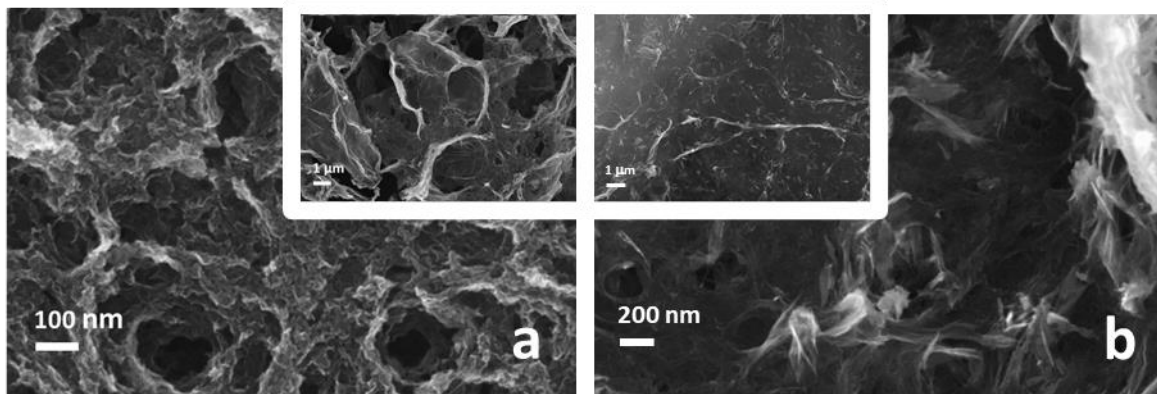
377 morphology, as it can be appreciated both at higher and lower magnification (inset). The occurrence

378 of NTs interacting with the rGO matrix may be appreciated in Figure 5b, showing a good dispersion

379 of the NTs, likely aggregated in bundles, within the rGO flakes, both at higher and lower (inset)

380 magnification.

381

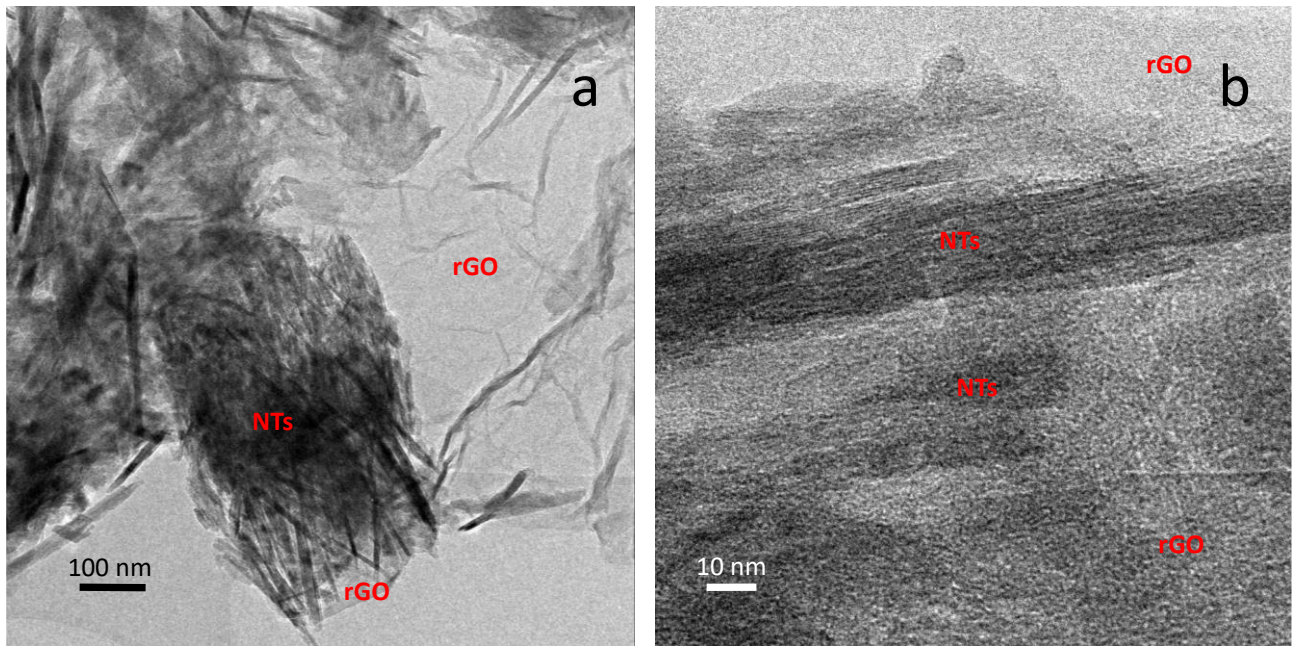


382

383 **Figure 5.** Selected FESEM micrographs of the parent rGO (a) and the rGO/Fe1.4-MeIMO  
 384 nanocomposite (b).

385

386 The interaction between the Fe2.8-MeIMO NTs and rGO was further verified by HRTEM  
 387 measurements on the rGO/Fe2.8-MeIMO nanocomposite (Figure 6), which put in evidence that the  
 388 NTs bundles and rGO are finely inter-dispersed, as also confirmed by EDX analysis (data not shown).  
 389 In this case, at variance with what was previously observed with the Fe1.4x2-MeIMO and Fe2.8-  
 390 MeIMO samples, the NTs were prevalently embedded within the rGO matrix, mostly as bundles or  
 391 aggregates of bundles, in agreement with the adopted synthesis procedure. Figure 6a shows very  
 392 likely aggregates of bundles embedded in the rGO, whereas Figure 6b allows appreciating bundles of  
 393 NTs dispersed in the rGO matrix.



394

395 **Figure 6.** Representative HRTEM images of the rGO/Fe<sub>2.8</sub>-MeIMO nanocomposite at low (a) and  
396 high magnification (b) in which the NTs appear as enveloped by the rGO flakes. Instrumental  
397 magnification is 50,000 $\times$  and 150,000 $\times$ , respectively.

398

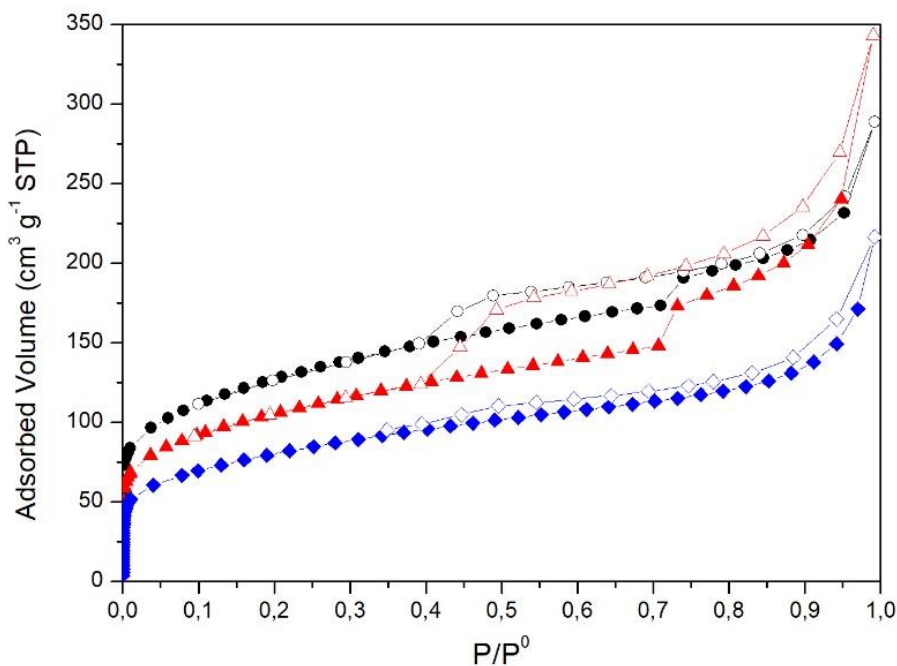
399 The effect of the Fe-doped MeIMO NTs on the porous structure of rGO was also assessed by  
400 measuring their N<sub>2</sub> isotherms at - 196 °C (Figure 7). The isotherm of the pristine rGO aerogel shows  
401 an adsorption branch composed of Type I(b) (low P/P<sup>0</sup> region, associated with micropores filling)  
402 and Type IV (high P/P<sup>0</sup> region, associated with mesopores filling) isotherms, with a limited hysteresis  
403 loop. The latter shows a lower limit of the desorption branch located at the cavitation-induced P/P<sup>0</sup>  
404 (ca. 0.4) and is likely given by non-rigid aggregates of rGO sheets (Gigot et al., 2016). A similar  
405 isotherm shape is observed with the rGO/Fe<sub>1.4</sub>-MeIMO nanocomposite, but in this case, a more  
406 complex hysteresis loop is present, as given by the overlapping of the two loops, specific to each  
407 parent nanomaterial. In contrast, the rGO/Fe<sub>2.8</sub>-MeIMO nanocomposite shows a very limited  
408 hysteresis loop (as also observed in the Fe<sub>2.8</sub>-MeIMO NTs alone). The fine dispersion of NTs bundles  
409 within the rGO matrix (as evidenced by HRTEM) could contribute to this feature.

410 The NTs addition to rGO brings about a decrease of the BET SSA, from 458 m<sup>2</sup>g<sup>-1</sup> (pristine  
 411 rGO aerogel) to 370 and 284 m<sup>2</sup>g<sup>-1</sup> (rGO/Fe1.4-MeIMO and rGO/Fe2.8-MeIMO, respectively). The  
 412 decrease in surface area is accompanied by a decrease in total porous volume and microporous  
 413 volume (Table 2). This feature, apparently in contrast to the high SSA of the parent Fe-doped NTs,  
 414 is mainly due to the lower outgassing temperature adopted with the studied aerogels. As reported in  
 415 the Experimental Section, to preserve the porous architecture of the freeze-dried aerogels, an  
 416 outgassing temperature of 150°C was adopted, whereas in previous work it was shown that both SSA  
 417 and total pore volume of Me-IMO NTs are halved when the outgassing temperature is lowered from  
 418 300 to 150°C (Bottero et al., 2011).

419

420 **Table 2.** BET SSA and micropore area (m<sup>2</sup> g<sup>-1</sup>), total pore volume and micropore volume (cm<sup>3</sup>  
 421 g<sup>-1</sup>) of rGO aerogel and the rGO/NTs nanocomposites as derived from N<sub>2</sub> sorption isotherms at -196  
 422 °C.

Sample	BET SSA (m <sup>2</sup> g <sup>-1</sup> )	Total pore volume (cm <sup>3</sup> g <sup>-1</sup> )
	Micropore area (m <sup>2</sup> g <sup>-1</sup> )	Micropore volume (cm <sup>3</sup> g <sup>-1</sup> )
rGO	458	0.45
	139	0.08
rGO/Fe1.4-MeIMO	370	0.53
	117	0.05
rGO/Fe2.8-MeIMO	284	0.33
	60	0.03



423

424 **Figure 7.** N<sub>2</sub> isotherms at -196 °C of pristine rGO (black circles), rGO/Fe1.4-MeIMO (red triangles)  
 425 and rGO/Fe2.8-MeIMO (blue diamonds).

426

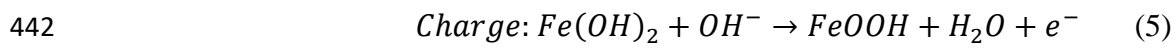
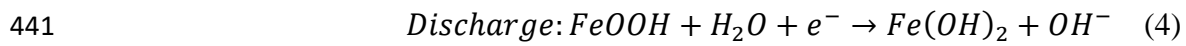
### 427 3.3 Electrochemical characterization

428 Electrochemical measurements were carried out in a three-electrode cell, as described in the  
 429 experimental section. Cyclic voltammetry was performed in 2.0 M KOH firstly at 2 mV s<sup>-1</sup> until stable  
 430 voltammograms have been obtained, and then at higher scan rates.

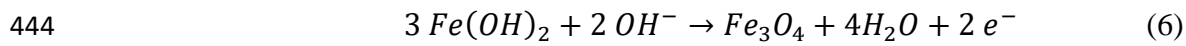
431 Figure 8a shows typical stable cyclic voltammograms obtained by sweeping the scan rate  
 432 between 0.1 and -1.6 V vs Ag/AgCl: MeIMO produced the blue voltammogram, which is  
 433 characterized by a fair capacitive behaviour, evidenced by the presence of the well-known rectangular  
 434 hysteresis, but also a strong resistive behaviour, evidenced by the linearization and tilting of the  
 435 voltammogram. Fe-doping produced an increase in the conductivity of the nanomaterial (by a  
 436 reduction of the tilt angle, clearly seen with the Fe1.4-MeIMO sample) and a larger and more stable

437 capacitance, clearly seen in the almost constant anodic current onto which small redox peaks appear  
438 (as seen with the Fe2.8-MeIMO sample).

439 According to the literature (Xia et al., 2016), the observed peaks refer to the following Fe  
440 reversible redox processes (eq. 4-6):

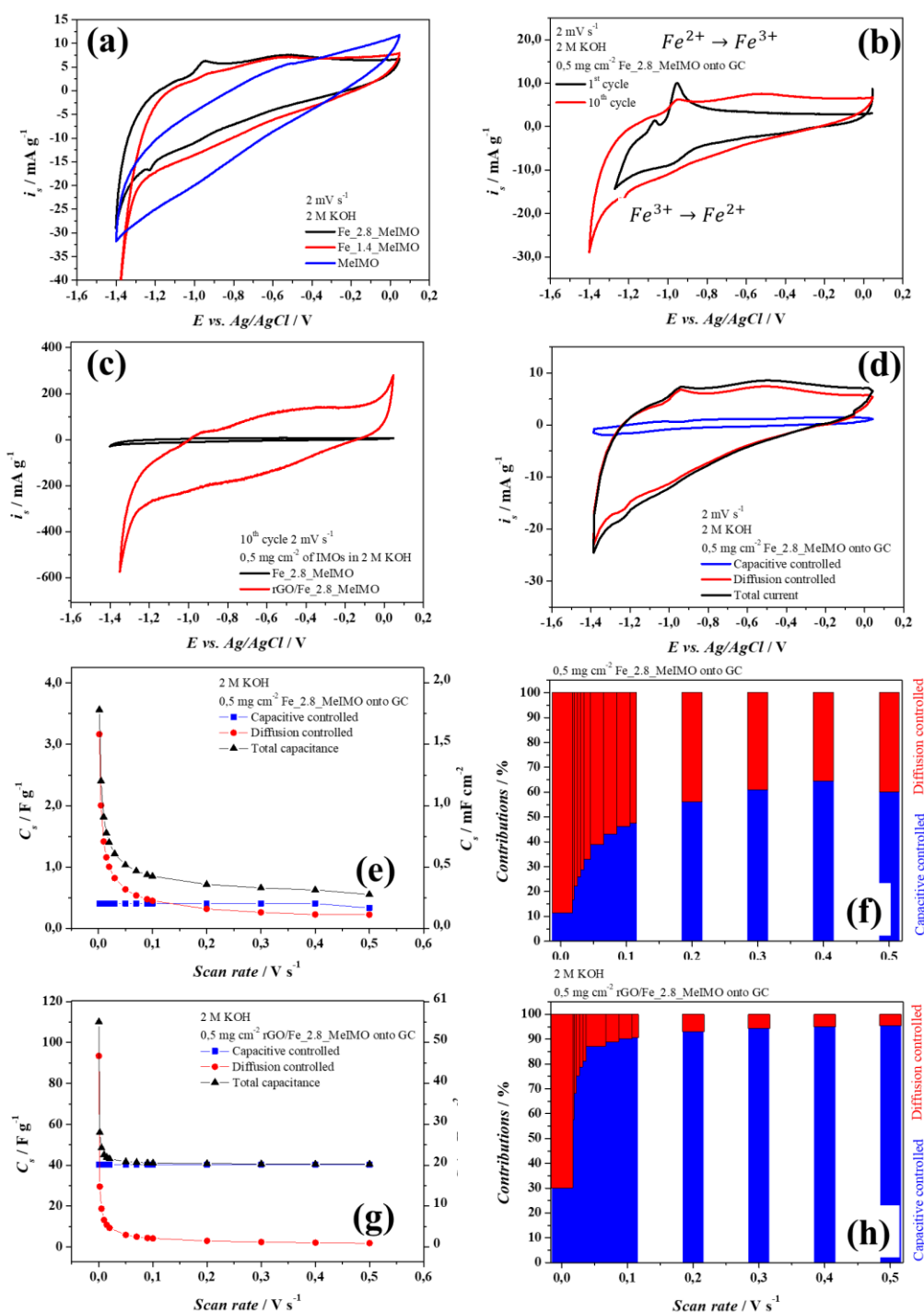


443 and/or



445

446



447

448 **Figure 8.** Section a): cyclic voltammetry at  $2 \text{ mV s}^{-1}$  recorded at the 10<sup>th</sup> cycle with the following  
 449 samples: Fe2.8MeIMO (black curve), Fe1.4MeIMO (red curve) and MeIMO (blue curve). Section  
 450 b): cyclic voltammetry recorded at the 1<sup>st</sup> cycle (black curve) and 10<sup>th</sup> cycle (red curve) with the  
 451 Fe2.8MeIMO sample. Section c): cyclic voltammetry recorded at the 10<sup>th</sup> cycle with the

452 Fe<sub>2.8</sub>MeIMO (black curve) and rGO/Fe<sub>2.8</sub>MeIMO nanocomposite (red curve). Sections d), e) and f)  
453 are those on the sample Fe<sub>2.8</sub>MeIMO and they show d) the reconstructed capacitive-controlled (blue  
454 curve) and diffusion-controlled (red curve) voltammeteries compared to the raw data (black curve)  
455 estimated at 2 mV s<sup>-1</sup>; e) the rate capabilities and f) the percentage of the capacitive-controlled and  
456 diffusion-controlled charges at different scan rates. Sections g) and h) show the rate capabilities and  
457 the percentage of the capacitive-controlled and diffusion-controlled charges at different scan rates for  
458 the rGO/Fe<sub>2.8</sub>MeIMO nanocomposite.

459

460 In Figure 8a, the stable cyclic voltammetry curves are reported, as obtained after 10 cycles.  
461 The first cycle appears, instead, quite different and both smaller capacitance (smaller hysteresis) and  
462 larger peaks are clear, as reported in Figure 8b. According to the literature, this phenomenon is an  
463 activation process from Fe<sub>2</sub>O<sub>3</sub> to FeOOH described by eq. 7:



465 Such an activation process is visible when cyclic voltammetry is performed on the Fe-doped MeIMO,  
466 but when the NTs are embedded in the 3D structure of rGO, the phenomenon is no more visible: in  
467 Figure 8c the voltammograms at the tenth cycle of the Fe<sub>2.8</sub>MeIMO sample and the  
468 rGO/Fe<sub>2.8</sub>MeIMO nanocomposite are compared, showing the enhancement of the capacitance of the  
469 latter sample at the electrode, in agreement with the fact that the CV plot of the bare rGO (not  
470 reported) showed a box-like shape, typical of the ideal capacitive behaviour of the material (Gigot et  
471 al., 2016).

472 The kinetic analysis performed on the Fe<sub>2.8</sub>MeIMO sample and the rGO/Fe<sub>2.8</sub>MeIMO  
473 nanocomposite allowed the appreciation of the effect that rGO made on the electrochemical behaviour  
474 of the Fe-doped MeIMO. According to Dunn's method (Wang et al., 2007), voltammograms acquired  
475 at different scan rates were analysed to retrieve the capacitive-controlled and diffusion-controlled

476 currents characteristic of each material. The current  $i(V)$  at each scan rate ( $\nu$ ) therefore follows eq.  
477 8 (Bard and Faulkner, 2000):

$$478 \quad i(V) = k_a \nu + k_b \nu^{1/2} \quad (8)$$

479 Figure 8d reports, as an example, the reconstructed voltammetry at  $2 \text{ mV s}^{-1}$  of the  
480 Fe<sub>2.8</sub>MeIMO sample showing the measured voltammetry (black curve), and the reconstructed  
481 voltammetry accounting for capacitive current (blue curve) and diffusion-controlled current (red  
482 curve) as calculated according to eq. 8. With the same code of colours, in Figures 8e-8h the rate  
483 capability test is presented as the usual plot of capacitance *versus* scan rate and as histograms,  
484 respectively, showing the percentage of capacitive-controlled and diffusion-controlled charges at  
485 each scan rate. By comparing this data analysis of the Fe<sub>2.8</sub>MeIMO sample with that of the  
486 rGO/Fe<sub>2.8</sub>MeIMO sample in Figure 8f and 8h, we can appreciate not only that the capacitance  
487 increases due to the presence of the rGO 3D structure, but also that the efficiency in the surface  
488 utilization of the Fe<sub>2.8</sub>MeIMO sample increases, leading to a clear enhancement of 1 order of  
489 magnitude (at  $2 \text{ mV s}^{-1}$ , from 3 to  $\approx 90 \text{ F g}^{-1}$ ) of the diffusion-controlled charges, assuming that the  
490 totality of the current is produced by the Fe-doped MeIMO NTs alone.

491

## 492 **Conclusions**

493 Fe-doped methylimogolite NTs with an iron content of 1.4 and 2.8 wt.% were synthesized by  
494 following a simple ionic exchange procedure of preformed methylimogolite NTs in water suspension.  
495 In this way, FeOOH clusters decorating the outer surface of preformed NTs were obtained, showing  
496 a redox response as measured by Cyclic Voltammetry. The interaction with the NTs matrix allowed  
497 stabilization of the clusters and favoured their dispersion, preventing aggregation phenomena that  
498 could lower the electrochemical response.

499           Successively, rGO/Fe-doped NTs were obtained for the first time by a facile and environment-  
500 friendly hydrothermal process followed by a freeze-drying procedure, which allowed reaching an  
501 effective dispersion of the NTs among the rGO flakes interconnected each other in a 3D porous  
502 architecture, as testified by electron microscopies. This nanocomposite material clearly shows an  
503 enhanced electrochemical response, thanks to the cooperation between the rGO properties, widely  
504 exploited in the last decade in the production of electrodes for energy storage devices, and the redox  
505 properties of Fe-doped NTs of the imogolite type. The latter had been already studied in Fe-modified  
506 imogolite NTs (Castro et al., 2016), showing that electrodes modified with imogolite and Fe-modified  
507 imogolite showed an increased electrochemically-active surface area (increased capacitive current).

508           The nanocomposites developed in this work, offering chemical stability, high surface area and  
509 the possibility to stabilize electrochemically active Fe species, could become a platform on which to  
510 disperse/support several types of electrocatalysts (e.g., Fe phthalocyanines) for relevant reactions,  
511 like oxygen reduction, for instance.

512

## 513 **Acknowledgements**

514           Dr Roberto Nasi (Department of Applied Science and Technology, Politecnico di Torino) is  
515 acknowledged for performing the ionic exchange of the Fe<sub>1.4x2</sub>-MeIMO and the Fe<sub>2.8</sub>-MeIMO  
516 samples.

517           Dr Arnaud Gigot (Department of Applied Science and Technology, Politecnico di Torino) is  
518 acknowledged for contributing to developing and performing the hydrothermal process to obtain the  
519 Fe doped-MeIMO/rGO nanocomposites.

520

## 521 **References**

522 Ackerman, W.C., Smith, D.M., Huling, J.C., Kim, Y.W., Bailey, J.K., Brinker, C.J., 1993.  
523 Gas/vapor adsorption in imogolite: a microporous tubular aluminosilicate. *Langmuir* 9,  
524 1051–1057. <https://doi.org/10.1021/la00028a029>

525 Alvarez-Ramírez, F., 2009. First principles studies of Fe-containing aluminosilicate and  
526 aluminogermanate nanotubes. *J. Chem. Theory. Comput.* 5, 3224–3231.  
527 <https://doi.org/10.1021/ct9004992>

528 Amara, M.S., Paineau, E., Rouzière, S., Guiose, B., Krapf, M.-E.M., Taché, O., Launois, P.,  
529 Thill, A., 2015. Hybrid, tunable-diameter, metal oxide nanotubes for trapping of organic  
530 molecules. *Chemistry of Materials* 27, 1488–1494. <https://doi.org/10.1021/cm503428q>

531 Armandi, M., Bonelli, B., Karaindrou, E.I., Areán, C.O., Garrone, E., 2008. Post-synthesis  
532 modifications of SBA-15 carbon replicas: Improving hydrogen storage by increasing  
533 microporous volume. *Catal. Today* 138, 244–248.  
534 <https://doi.org/10.1016/j.cattod.2008.05.002>

535 Avellan, A., Levard, C., Kumar, N., Rose, J., Olivi, L., Thill, A., Chaurand, P., Borschneck,  
536 D., Masion, A., 2014. Structural incorporation of iron into Ge-imogolite nanotubes: a  
537 promising step for innovative nanomaterials. *RSC Advances* 4, 49827–49830.  
538 <https://doi.org/10.1039/C4RA08840A>

539 Bahadori, E., Vaiano, V., Esposito, S., Armandi, M., Sannino, D., Bonelli, B., 2018. Photo-  
540 activated degradation of tartrazine by H<sub>2</sub>O<sub>2</sub> as catalyzed by both bare and Fe-doped  
541 methyl-imogolite nanotubes. *Catal. Today* 304, 199–207.  
542 <https://doi.org/10.1016/j.cattod.2017.08.003>

543 Bard, A.J., Faulkner, L.R., 2000. *Electrochemical methods: fundamentals and applications*,  
544 2nd Edition. ed.

545 Bonelli, B., Armandi, M., Garrone, E., 2013a. Surface properties of alumino-silicate single-  
546 walled nanotubes of the imogolite type. *Phys. Chem. Chem. Phys.*, 15, 13381–13390.  
547 <https://doi.org/10.1039/c3cp51508g>

548 Bonelli, B., Bottero, I., Ballarini, N., Passeri, S., Cavani, F., Garrone, E., 2009. IR  
549 spectroscopic and catalytic characterization of the acidity of imogolite-based systems. *J.*  
550 *Catal.* 264, 15–30. <https://doi.org/10.1016/j.jcat.2009.03.003>

551 Bonelli, B., Zanzottera, C., Armandi, M., Esposito, S., Garrone, E., 2013b. IR spectroscopic  
552 study of the acidic properties of alumino-silicate single-walled nanotubes of the imogolite  
553 type. *Catal. Today* 218–219, 3–9. <https://doi.org/10.1016/j.cattod.2013.02.004>

554 Bottero, I., Bonelli, B., Ashbrook, S.E., Wright, P.A., Zhou, W., Tagliabue, M., Armandi, M.,  
555 Garrone, E., 2011. Synthesis and characterization of hybrid organic/inorganic nanotubes  
556 of the Imogolite type and their behaviour towards methane adsorption. *Phys. Chem.*  
557 *Chem. Phys.* 13, 744–750. <https://doi.org/10.1039/c0cp00438c>

558 Bursill, L.A., Peng, J.L., Bourgeois, L.N., 2000. Imogolite: An aluminosilicate nanotube  
559 material. *Philos. Mag. A* 80, 105–117. <https://doi.org/10.1080/01418610008212043>

560 Castro, C., Arancibia-Miranda, N., Acuña-Rougier, C., Escudey, M., Tasca, F., 2016.  
561 Spectroscopic and electrochemical studies of imogolite and Fe-modified Imogolite  
562 nanotubes. *Nanomaterials* 6(2), 28. <https://doi.org/10.3390/nano6020028>

563 Cradwick, P.D.G., Farmer, V.C., Russell, J.D., Masson, C.R., Wada, K., Yoshinaga, N., 1972.  
564 Imogolite, a hydrated aluminium silicate of tubular structure. *Nature Physical Science*  
565 240, 187–189. <https://doi.org/10.1038/physci240187a0>

566 Creton, B., Bougeard, D., Smirnov, K.S., Guilment, J., Poncelet, O., 2008. Molecular  
567 dynamics study of hydrated imogolite. *Phys. Chem. Chem. Phys.* 10, 4676–4677.  
568 <https://doi.org/10.1039/b812223g>

569 D'Angelo, A., Paineau, E., Rouzière, S., Elkaim, É., Goldmann, C., Toquer, D., Rols, S.,  
570 Launois, P., 2023. The atomic structure of imogolite nanotubes: A 50 years old issue  
571 reinvestigated by X-ray scattering experiments and molecular dynamics simulations.  
572 *Appl Clay Sci* 242, 107043. <https://doi.org/10.1016/j.clay.2023.107043>

573 Farmer, V.C., Fraser, A.R., 1978. Synthetic imogolite, a tubular hydroxyaluminum silicate, in:  
574 *Proc. Int. Clay Conf.*, Oxford. pp. 547–553.

575 Fernandez-Martinez, A., Michot, L.J., 2016. Physicochemical properties of imogolite, in:  
576 Yuan, P., Thill, A., Bergaya, F. (Eds.), *Developments in Clay Science*. Bergaya, F. , pp.  
577 202–222. <https://doi.org/10.1016/B978-0-08-100293-3.00009-1>

578 Gigot, A., Fontana, M., Serrapede, M., Castellino, M., Bianco, S., Armandi, M., Bonelli, B.,  
579 Pirri, C., Tresso, E., Rivolo, P., 2016. Mixed 1T–2H phase MoS<sub>2</sub>/reduced Graphene  
580 Oxide as active electrode for enhanced supercapacitive performance. *ACS Appl. Mater.*  
581 *Interfaces* 8, 32842–32852. <https://doi.org/10.1021/acsami.6b11290>

582 Gorgolis, G., Galiotis, C., 2017. Graphene aerogels: a review. *2d Mater* 4.  
583 <https://doi.org/10.1088/2053-1583/aa7883>

584 Han, S., Wu, D., Li, S., Zhang, F., Feng, X., 2014. Porous graphene materials for advanced  
585 electrochemical energy storage and conversion devices. *Adv. Mater.* 26, 849–864.  
586 <https://doi.org/10.1002/adma.201303115>

587 Iwasaki, M., Yamazaki, K., Banno, K., Shinjoh, H., 2008. Characterization of Fe/ZSM-5  
588 DeNO<sub>x</sub> catalysts prepared by different methods: relationships between active Fe sites and  
589 NH<sub>3</sub>-SCR performance. *J Catal* 260, 205–216. <https://doi.org/10.1016/j.jcat.2008.10.009>

590 Kumar, M.S., Schwidder, M., Grünert, W., Bentrup, U., Brückner, A., 2006. Selective  
591 reduction of NO with Fe-ZSM-5 catalysts of low Fe content: Part II. Assessing the

592 function of different Fe sites by spectroscopic in situ studies. *J. Catal.* 239, 173–186.  
593 <https://doi.org/10.1016/j.jcat.2006.01.024>

594 Mackenzie, K.J.D., 1989. Structure and thermal transformations of imogolite studied by  $^{29}\text{Si}$   
595 and  $^{27}\text{Al}$  high-resolution solid-state Nuclear Magnetic Resonance. *Clay Clay Miner.* 37,  
596 317–324. <https://doi.org/10.1346/CCMN.1989.0370404>

597 Ma, L., Li, J., Arandiyana, H., Shi, W., Liu, C., Fu, L., 2012. Influence of calcination  
598 temperature on Fe/HBEA catalyst for the selective catalytic reduction of  $\text{NO}_x$  with  $\text{NH}_3$ ,  
599 in: *Catal. Today*. pp. 145–152. <https://doi.org/10.1016/j.cattod.2011.10.007>

600 Monet, G., Amara, M.S., Rouzière, S., Paineau, E., Chai, Z., Elliott, J.D., Poli, E., Liu, L.M.,  
601 Teobaldi, G., Launois, P., 2018. Structural resolution of inorganic nanotubes with  
602 complex stoichiometry. *Nat Commun* 9. <https://doi.org/10.1038/s41467-018-04360-z>

603 Nasi, R., Sannino, F., Picot, P., Thill, A., Oliviero, O., Esposito, S., Armandi, M., Bonelli, B.,  
604 2020. Hybrid organic-inorganic nanotubes effectively adsorb some organic pollutants in  
605 aqueous phase. *Appl. Clay Sci.* 186, 105449. <https://doi.org/10.1016/j.clay.2020.105449>

606 Picot, P., Gobeaux, F., Coradin, T., Thill, A., 2019. Dual internal functionalization of imogolite  
607 nanotubes as evidenced by optical properties of Nile red. *Appl. Clay Sci.* 178, 1015133.  
608 <https://doi.org/10.1016/j.clay.2019.105133>

609 Shafia, E., Esposito, S., Armandi, M., Bahadori, E., Garrone, E., Bonelli, B., 2016. Reactivity  
610 of bare and Fe-doped alumino-silicate nanotubes (imogolite) with  $\text{H}_2\text{O}_2$  and the azo-dye  
611 Acid Orange 7. *Catal. Today* 277, 89–96. <https://doi.org/10.1016/j.cattod.2015.10.011>

612 Shafia, E., Esposito, S., Manzoli, M., Chiesa, M., Tiberto, P., Barrera, G., Menard, G., Allia,  
613 P., Freyria, F.S., Garrone, E., Bonelli, B., 2015. Al/Fe isomorphic substitution versus  
614  $\text{Fe}_2\text{O}_3$  clusters formation in Fe-doped aluminosilicate nanotubes (Imogolite). *J. Nanopart.*  
615 *Res.* 17. <https://doi.org/10.1007/s11051-015-3130-2>

616 Tamang, S., Rai, S., Bhujel, R., Bhattacharyya, N.K., Swain, B.P., Biswas, J., 2023. A concise  
617 review on GO, rGO and metal oxide/rGO composites: fabrication and their supercapacitor  
618 and catalytic applications. *J. Alloys. Compd.*  
619 <https://doi.org/10.1016/j.jallcom.2023.169588>

620 Teobaldi, G., Beglitis, N.S., Fisher, A.J., Zerbetto, F., Hofer, W.A., 2008. Hydroxyl vacancies  
621 in single-walled aluminosilicate and aluminogermanate nanotubes. *J. Phys. Condens.*  
622 *Matter* 21, 195301. <https://doi.org/10.1088/0953-8984/21/19/195301>

623 Thommes, M., Kaneko, K., Neimark, A. V., Olivier, J.P., Rodriguez-Reinoso, F., Rouquerol,  
624 J., Sing, K.S.W., 2015. Physisorption of gases, with special reference to the evaluation of  
625 surface area and pore size distribution (IUPAC Technical Report). *Pure Appl. Chem.* 87,  
626 1051–1069. <https://doi.org/10.1515/pac-2014-1117>

627 Van Der Gaast, S.J., Wada, K., Wada, S.-I., Kakuto, Y., 1985. Small-angle X-ray powder  
628 diffraction, morphology, and structure of allophane and imogolite. *Clay Clay Miner.* 33,  
629 237–243.

630 Wada, K., Yoshinaga, N., Yotsumoto, H., Ibe, K., Aida, S., 1970. High resolution electron  
631 micrographs of imogolite. *Clay Miner.* 8, 487–489.

632 Wada, S.-I., Eto, A., Wada, K., 1979. Synthetic allophane and imogolite. *Journal of Soil*  
633 *Science* 30, 347–355. <https://doi.org/10.1111/j.1365-2389.1979.tb00991.x>

634 Wang, J., Polleux, J., Lim, J., Dunn, B., 2007. Pseudocapacitive contributions to  
635 electrochemical energy storage in TiO<sub>2</sub> (anatase) nanoparticles. *J. Phys. Chem. C* 111,  
636 14925–14931. <https://doi.org/10.1021/jp074464w>

637 Wang, Y., Zhang, L., Hou, H., Xu, W., Duan, G., He, S., Liu, K., Jiang, S., 2021. Recent  
638 progress in carbon-based materials for supercapacitor electrodes: a review. *J. Mater. Sci.*  
639 56, 173–200. <https://doi.org/10.1007/s10853-020-05157-6>

640 Wang, Y., Zhang, Q., Shishido, T., Takehira, K., 2002. Characterizations of iron-containing  
641 MCM-41 and its catalytic properties in epoxidation of styrene with hydrogen peroxide. *J.*  
642 *Catal.* 209, 186–196. <https://doi.org/10.1006/jcat.2002.3607>

643 Xia, Q., Xu, M., Xia, H., Xie, J., 2016. Nanostructured Iron oxide/hydroxide-based electrode  
644 materials for supercapacitors. *ChemNanoMat* 2, 588–600.  
645 <https://doi.org/10.1002/cnma.201600110>

646 Yoshinaga, N., Aomine, S., 1962. Imogolite in some ando soils. *Soil Sci Plant Nutr* 8, 22–29.  
647 <https://doi.org/10.1080/00380768.1962.10430993>

648 Zanzottera, C., Armandi, M., Esposito, S., Garrone, E., Bonelli, B., 2012a. CO<sub>2</sub> adsorption on  
649 aluminosilicate single-walled nanotubes of imogolite type. *J. Phys. Chem. C* 116, 20417–  
650 20425. <https://doi.org/10.1021/jp3061637>

651 Zanzottera, C., Vicente, A., Armandi, M., Fernandez, C., Garrone, E., Bonelli, B., 2012b.  
652 Thermal collapse of single-walled alumino-silicate nanotubes: transformation  
653 mechanisms and morphology of the resulting lamellar phases. *J. Phys. Chem. C* 116,  
654 23577–23584. <https://doi.org/10.1021/jp3090638>

655 Zanzottera, C., Vicente, A., Celasco, E., Fernandez, C., Garrone, E., Bonelli, B., 2012c.  
656 Physico-chemical properties of imogolite nanotubes functionalized on both external and  
657 internal surfaces. *J. Phys. Chem. C* 116, 7499–7506. <https://doi.org/10.1021/jp301177q>

658